Low-background neutron reflectometry from solid/liquid interfaces

David P. Hoogerheide,* Joseph A. Dura, Brian B. Maranville and Charles F. Majkrzak

Center for Neutron Research, National Institute of Standards and Technology, 100 Bureau Drive, Gaithersburg, MD 20899, USA. *Correspondence e-mail: david.hoogerheide@nist.gov

Liquid cells are an increasingly common sample environment for neutron reflectometry experiments and are critical for measuring the properties of materials at solid/liquid interfaces. Background scattering determines the maximum useful scattering vector, and hence the spatial resolution, of the neutron reflectometry measurement. The primary sources of background are the liquid in the cell reservoir and the materials forming the liquid cell itself. Thus, characterization and mitigation of these background sources are necessary for improvements in the signal-to-background ratio and resolution of neutron reflectometry measurements employing liquid cells. Single-crystal silicon is a common material used for liquid cells due to its low incoherent scattering cross section for neutrons, and the path lengths of the neutron beam through silicon can be several centimetres in modern cell designs. Here, a liquid cell is constructed with a sub-50 µm thick liquid reservoir encased in single-crystal silicon. It is shown that, at high scattering vectors, inelastic scattering from silicon represents a significant portion of the scattering background and is, moreover, structured, confounding efforts to correct for it by established background subtraction techniques. A significant improvement in the measurement quality is achieved using energy-analyzed detection. Energy-analyzed detection reduces the scattering background from silicon by nearly an order of magnitude, and from fluids such as air and liquids by smaller but significant factors. Combining thin liquid reservoirs with energy-analyzed detection and the high flux of the CANDOR polychromatic reflectometer at the NIST Center for Neutron Research, a background-subtracted neutron reflectivity smaller than 10^{-8} from a liquid cell sample is reported.

1. Introduction

Neutron reflectometry (NR) is a powerful method to interrogate the structure of multilayered thin films at interfaces and has found application in many areas in both hard and soft condensed matter. In specular NR, the neutron reflectivity $R(Q_z)$ is measured as the fraction of neutrons that reflect from a sample surface as a function of the momentum transfer of the reflection process, $Q_z = 4\pi\lambda^{-1}\sin(\theta)$, where λ is the neutron wavelength and θ is the angle of both incidence and reflection relative to the sample surface. $R(Q_z)$ reveals the underlying one-dimensional neutron scattering length density (nSLD) profile in the normal direction $\mathbf{z}$ to the sample surface, averaging over all lateral inhomogeneities. The nSLD profile encodes information regarding the composition and density of the thin-film materials; the spatial resolution, or the length scale below which variations in the nSLD profile can no longer be resolved, is determined by the maximum momentum transfer Q_z^{max} measured. In practice, $R(Q_z)$ falls off very quickly with Q_z, such that Q_z^{max} is the maximum momentum
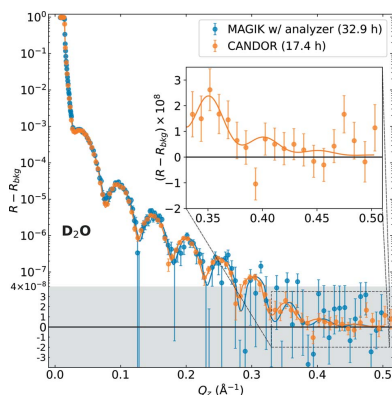
transfer at which the signal-to-noise ratio of the data is sufficient to constrain a real-space model of the nSLD profile.

Liquid cells are a common sample environment for NR applications involving solid/liquid interfaces (Hoogerheide, Heinrich et al., 2020). In NR measurements of electrochemical processes (Dura et al., 2017), for example, liquid cells enable the introduction (Rus & Dura, 2019) or exchange (Owejan et al., 2012) of electrolytes. Similarly, biological NR measurements typically employ liquid flow cells for assembly of the bilayer systems, as well as for the introduction of buffers and biological molecules (Eells et al., 2019). Biological membranes and their mimics are particularly well suited for study by NR due to their planar geometry and the sensitivity of neutrons to light elements, especially the isotopes of hydrogen, enabling opportunities for molecular perdeuteration or contrast variation of the surrounding buffer (Eells et al., 2019; Hoogerheide, Forsyth & Brown, 2020; Fitter et al., 2006; Ankner et al., 2013). These techniques are regularly deployed to probe adhesion of biomolecules and biomembranes to interfaces (Nylander et al., 2008; Michalak et al., 2021; Clifton et al., 2019; Fragneto et al., 2001), changes in bilayer morphology when exposed to small molecules or membrane-associated proteins (Paracini et al., 2018; Pfefferkorn et al., 2012; Mihailescu et al., 2019; Thorsen et al., 2021) or other physical or chemical perturbations (Junghans et al., 2015; Silin & Hoogerheide, 2021), structures of integral membrane proteins (McGillivray et al., 2009; Hoogerheide et al., 2018; Soranzo et al., 2017), and the structure and orientation of peripheral proteins (Heinrich & Lösche, 2014; Hoogerheide et al., 2017; Van et al., 2020; Soubias et al., 2020). Because many biomolecules have structures on the 1 nm length scale, e.g. protein α-helices or lipid headgroups, routinely achieving sub-nanometre spatial resolution would greatly enhance the information that could be gleaned from biological NR. To achieve a spatial resolution of 5 Å with measurements in two solvent contrast conditions (e.g. D_2O and H_2O) or reference substrates, the required $Q_z^{max} \simeq \pi/(5\,\text{Å}) = 0.6\,\text{Å}^{-1}$ (Berk & Majkrzak, 2003; Majkrzak et al., 2003; Schalke & Lösche, 2000), about double that typical for NR measurements. For a 50 Å thick lipid bilayer on a perfect silicon substrate immersed in D_2O, $R(0.6\,\text{Å}^{-1}) \simeq 10^{-7}$, thus defining the target background level for high-resolution measurement of biological systems.

In NR involving liquid cell samples, it has previously been shown that the liquid reservoir and the flow cell materials are the primary sources of background (Hoogerheide, Heinrich et al., 2020), and that, in the case where the background arises from isotropic scattering, the background field can be described and subtracted with high accuracy and limited measurement time. Reducing the liquid reservoir thickness was also found to have the most effect on the overall background level for liquid cell designs in which the substrate materials do not scatter strongly (Hoogerheide, Heinrich et al., 2020).

In this work, we used a liquid cell constructed from silicon substrates separated by a very thin, sub-50 μm, liquid reservoir to resolve features in the neutron reflectivity pattern at the $R < 10^{-8}$ level. First, we show that inelastic scattering processes play an additional confounding role for high-Q_z measurement. The non-isotropic nature of inelastic scattering is particularly apparent when the liquid cell is constructed from single-crystal silicon, which is a widespread practice due to its low incoherent scattering cross section and wide availability. Non-isotropic inelastic scattering is particularly problematic because it is difficult to account for using background interpolation or background field subtraction techniques (Hoogerheide, Heinrich et al., 2020) without introducing 'spurion' features that are difficult to distinguish from the specular neutron reflectivity. Second, we present data suggesting that the observed spurions, which are present at the small but significant level of 4×10^{-7}, arise from multiple scattering events involving silicon phonons and Bragg reflections. Third, we show that the introduction of an energy analyzer in a monochromatic NR experiment effectively filters the inelastically scattered neutrons and removes the spurion signal completely. Finally, we demonstrate reflectivity at the 10^{-8} level from a liquid cell using the high-flux CANDOR reflectometer with its intrinsically energy-analyzed detector.

2. Methods

The experimental setup of the MAGIK (previously AND/R) reflectometer is shown in Fig. 1(a). A polychromatic beam produced by the National Bureau of Standards Reactor (NBSR) and moderated by a liquid H_2 cold source (Kopetka et al., 2006) impinges on a triple-blade focusing monochromator located in Neutron Guide D that selects $\lambda = 5$ Å neutrons with $\Delta\lambda/\lambda = 0.0090$ (Dura et al., 2006). The monochromatic beam passes through two pre-sample collimating slits (slits 1 and 2) before arriving at the sample position. The sample surface is oriented at an angle θ relative to the incident beam. The detector arm comprises two post-sample collimating slits (slits 3 and 4) and the detector apparatus. The angle of the detector arm relative to the incident beam is Δ.

For the measurements described in this article, the MAGIK detector comprises two components, a single-blade highly oriented pyrolytic graphite (HOPG) analyzer and a 25.4 mm diameter helium tube detector. Each of these is mounted on a rotation stage. The HOPG analyzer is 'in' [Fig. 1(b)] when rotated to an angle $\theta_{analyzer}$ relative to the scattered beam and the helium tube is rotated to an angle $2\theta_{analyzer}$. In this case the detector is sensitive only to neutrons that are Bragg scattered from the HOPG analyzer with wavelength $\lambda_f = 2d_{HOPG} \times \sin(\theta_{analyzer})$, where d_{HOPG} (= 3.354 Å) is the graphite plane spacing.

The HOPG analyzer is 'out' [Fig. 1(c)] when the helium tube is in line with the scattered beam path defined by slits 3 and 4 while the analyzer is rotated to 90° such that the beam passes through the HOPG analyzer and impinges directly on the helium tube. In this case, the detector is sensitive to neutrons over a broad wavelength band. Note that because the MAGIK monochromator comprises three HOPG blades that slightly overlap in their mosaic angular distribution, such that the assembly has 2.6 times the wavelength divergence of a

single blade, a 2.6-fold decrease in intensity is observed when the single HOPG analyzer crystal is in.

The CANDOR reflectometer [Fig. 1(d)] operates under a similar principle, except that the wavelength selection is done in the detector (Maliszewskyj et al., 2018). A polychromatic beam from the NBSR cold source traveling through Neutron Guide 1 impinges on the pre-sample collimating slits, the sample and the post-sample collimating slits before entering the detector [Fig. 1(e)]. The CANDOR detector is a channel with an array of 54 single-blade HOPG crystals in series at fixed angles to select neutrons in the 4–6 Å wavelength range. As the polychromatic scattered beam passes each crystal, neutrons of the corresponding wavelength are diffracted into scintillation detectors (Pritchard et al., 2020) located along the side of the channel [the bottom solid line in Fig. 1(e)]. Thus, CANDOR operates as a multiplexed monochromatic reflectometer with built-in energy-analyzed detection. At matched Q_z resolution, the neutron detection rate on CANDOR is about 22 times higher than that on MAGIK, consistent with the 54-fold multiplexing and the 2.6-fold loss in wavelength spread for each detector relative to the MAGIK triple-blade monochromator.

The reflectivity of the sample as measured by either reflectometer is defined as

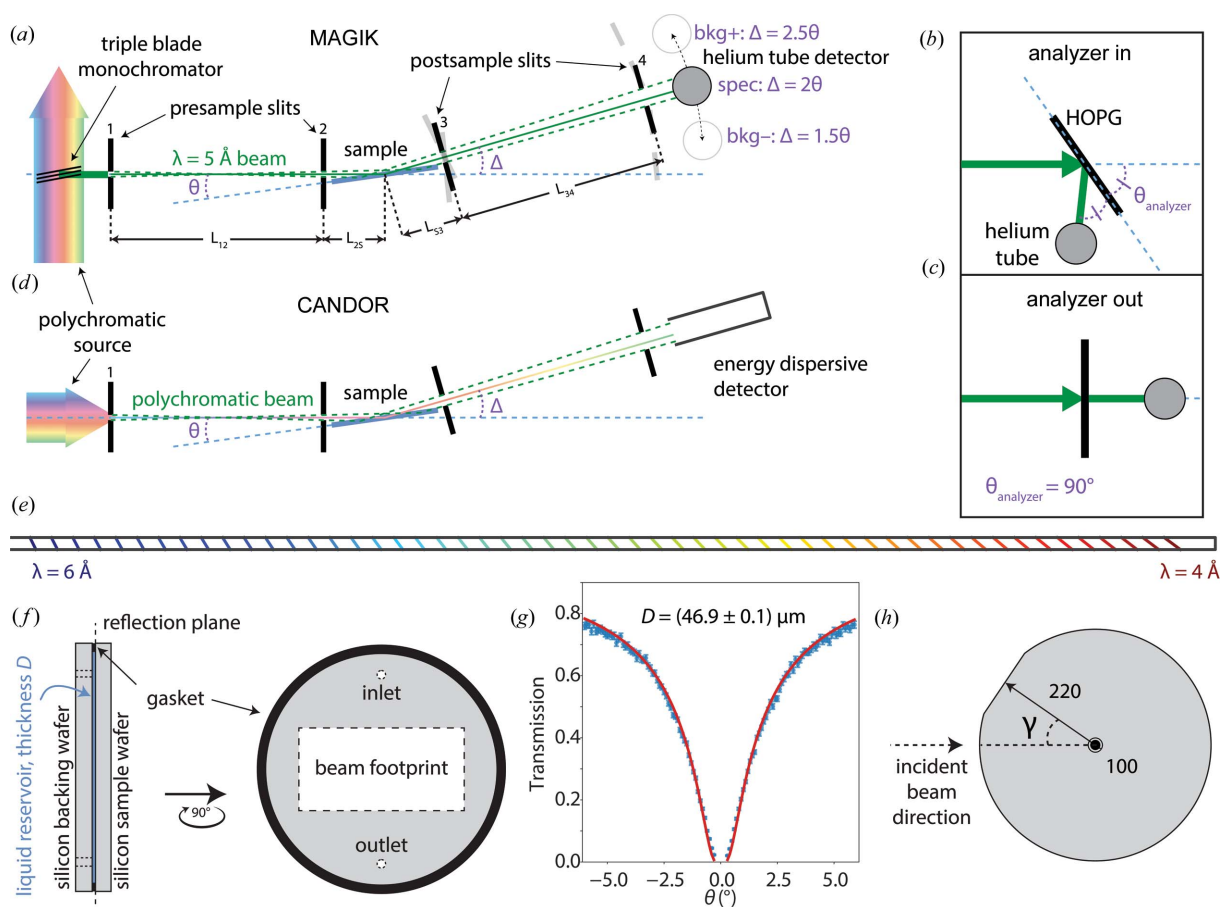$$R(Q_z) = \frac{I_{\mathrm{spec}}(Q_z) - 0.5\big[I_{\mathrm{bkg}+}(Q_z) + I_{\mathrm{bkg}-}(Q_z)\big]}{I_0(Q_z)}. \quad (1)$$

Figure 1
Experimental setup. (a)–(c) MAGIK reflectometer operation. (a) A λ = 5 Å beam is selected from a polychromatic source in the neutron guide with a triple-blade monochromator ($\Delta\lambda/\lambda \simeq 0.9\%$). With the sample rotated to an angle θ relative to the incident beam, specular reflection occurs at a detector rotation angle Δ. The collimation determines the width of the beam, shown as dashed lines. In this diagram, which is not to scale, the asymmetry in the beam is exaggerated by the oversized sample and large reflection angles. Background subtraction is performed by interpolation between intensities measured with the detector rotated to either side of the specular ridge. (b), (c) Implementation of energy analysis on MAGIK using an HOPG analyzer crystal. (b) When the analyzer is 'in', the HOPG analyzer is rotated to $\theta_{\mathrm{analyzer}}$ and the helium tube to $2\theta_{\mathrm{analyzer}}$, selecting a wavelength $\lambda_f = 2d_{\mathrm{HOPG}}\sin(\theta_{\mathrm{analyzer}})$. (c) When the analyzer is 'out', $\theta_{\mathrm{analyzer}} = 90°$ and the helium tube is at $0°$, i.e. in the path of scattered neutrons of all wavelengths. (d) The CANDOR reflectometer operates similarly to MAGIK but effectively acts as 54 independent energy-analyzed reflectometers. The physical length of the CANDOR reflectometer is also approximately 2.5 times that of MAGIK. (e) A schematic diagram of the CANDOR detector. Individual HOPG blades diffract neutrons of the appropriate wavelength into scintillation detectors and are colored according to the 'temperature' of the selected neutrons. (f) The geometry of the flow cell. A thin liquid reservoir is created in the space between two silicon wafers separated by a thin Teflon gasket. The presample slit openings are proportional to $\sin(\theta)$ so the beam footprint on the sample remains constant. (g) The thickness D of the liquid reservoir is determined by measuring the angle-dependent transmission of neutrons through an H_2O-filled reservoir. Error bars represent a 68% confidence interval derived from the Poisson-distributed uncertainty in the neutron counts. (h) The nominal crystal orientation of the silicon wafer. The flat denotes the [220] direction and is rotated at an angle γ relative to the beam direction.

Here, the nominal momentum transfer of the reflection process is $Q_z = 4\pi\lambda^{-1}\sin(\theta)$, the z axis is defined normal to the sample surface and Q_z is defined by the sample rotation θ. $I_{\mathrm{spec}}(Q_z)$ is the specular intensity measured when $\Delta = 2\theta$, while $I_{\mathrm{bkg+}}(Q_z)$ and $I_{\mathrm{bkg-}}(Q_z)$ are background intensities measured at the positions $\Delta = 2.5\theta$ and $\Delta = 1.5\theta$, respectively. For each individual measurement, the pre- and post-sample collimating slits are adjusted to maintain a constant beam footprint on the sample [Fig. 1(f)]; exact expressions can be found in the paper by Hoogerheide, Heinrich et al. (2020) and additional practical aspects of neutron reflectometry can be found in the reports by Dura et al. (2017) and Eells et al. (2019). The background subtraction in equation (1) implements a linear interpolation scheme described previously (Hoogerheide, Heinrich et al., 2020); the non-isotropic background to be described here precludes the use of background field subtraction. The incident intensity, $I_0(Q_z)$, is measured with $\theta = 0$ and $\Delta = 0$, with the sample translated out of the beam such that the beam is passing through the incident material (silicon or air); the pre- and post-sample collimation are adjusted to match those of the specular and background intensity measurements at the same nominal Q_z. For MAGIK, the intensities were normalized to a beam monitor to correct for fluctuations in beam current; for CANDOR, the intensities are normalized only to counting time. All data presented are corrected for the dark count rate specific to the instrument configuration. Data reduction was performed using Reductus (Maranville et al., 2018)

The NIST liquid flow cell [Fig. 1(f)] comprises a thin reservoir of liquid confined between two silicon substrates that are separated with a Teflon gasket and externally clamped (Fig. S1 in the supporting information). The beam is incident through the 5 mm thick and 76.2 mm diameter sample substrate, which presents the interface of interest to the liquid in the reservoir; the opposing 9 mm thick 'backing' substrate contains two inlets allowing solution exchange over the course of the experiment. The pre-sample collimation constrains the beam footprint to an area of 25×45 mm on the sample substrate. The thickness of the liquid reservoir was determined from the angle-dependent transmission of the beam through H_2O [Fig. 1(g)]; the expression is

$$\frac{I(\theta)}{I_0} = \exp\left[-\frac{\epsilon_{\mathrm{H2O}}D}{\sin(\theta)}\right], \qquad (2)$$

where $\epsilon_{\mathrm{H2O}} = 5.435$ cm^{-1} is the previously determined attenuation coefficient of 5 Å neutrons through H_2O (Hoogerheide, Heinrich et al., 2020; Sears, 1992). Data with $|\theta| < 0.25°$ are excluded to avoid corrections for reflected neutrons. Equation (2) was optimized with the single free parameter D to the experimental data using a Levenberg–Marquardt algorithm, yielding $D = 46.9 \pm 0.1$ µm. Here, the error bar represents the 68% confidence interval of the thickness as determined from the covariance matrix.

The sample substrates are 5 mm thick and 76.2 mm diameter n-doped 100 single-crystal silicon, with a flat corresponding to the [220] direction [Fig. 1(h)]. The substrates were mounted such that the incident beam was oriented relative to the surface normal of the flat by an angle γ.

3. Results

A 120 Å thin film of SiO_2 was grown on a 100 silicon substrate by a dry thermal oxide process at the NIST Center for Nanoscale Science and Technology. The coated substrate was mounted in the NIST liquid cell as shown in Fig. 1(f) with $\gamma \simeq 0°$. The reflectivity was measured to $Q_z^{\mathrm{max}} = 0.5$ Å^{-1} on the MAGIK reflectometer with both D_2O [Fig. 2(a)] and H_2O [Fig. 2(b)] in the liquid reservoir and with the energy analyzer in both the in ($\lambda_{\mathrm{f}} = 5$ Å) and out (all λ) configurations. The differences in the measurements obtained using the two detection configurations are particularly striking in the D_2O
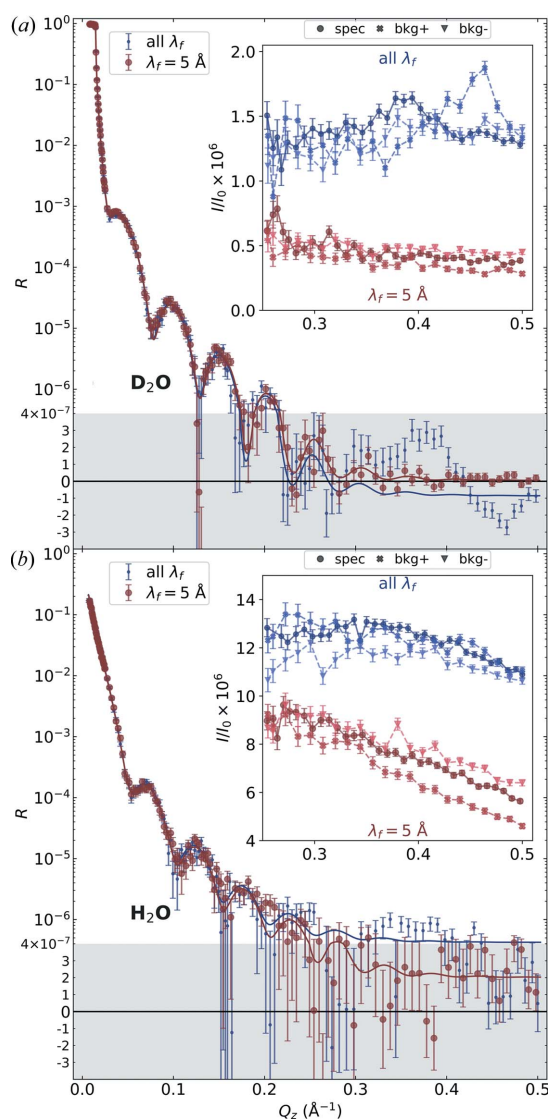
Figure 2
Neutron reflectivity of an SiO_2 thin film on a sample substrate mounted in a liquid cell such that $\gamma = 0°$. The liquid reservoir contained either (a) D_2O or (b) H_2O. Measurements were performed with the MAGIK reflectometer with ($\lambda_{\mathrm{f}} = 5$ Å) and without (all λ_{f}) energy-analyzed detection. Solid lines show the results of optimizing the experimental data to a single thin-film model ($Q_z > 0.25$ Å^{-1} data are excluded for data collected without energy analysis). Insets show individual intensity-normalized specular (spec) and background (bkg+ and bkg−) intensities. Shaded areas are plotted on a linear scale. Error bars represent 68% confidence intervals of the reduced data.
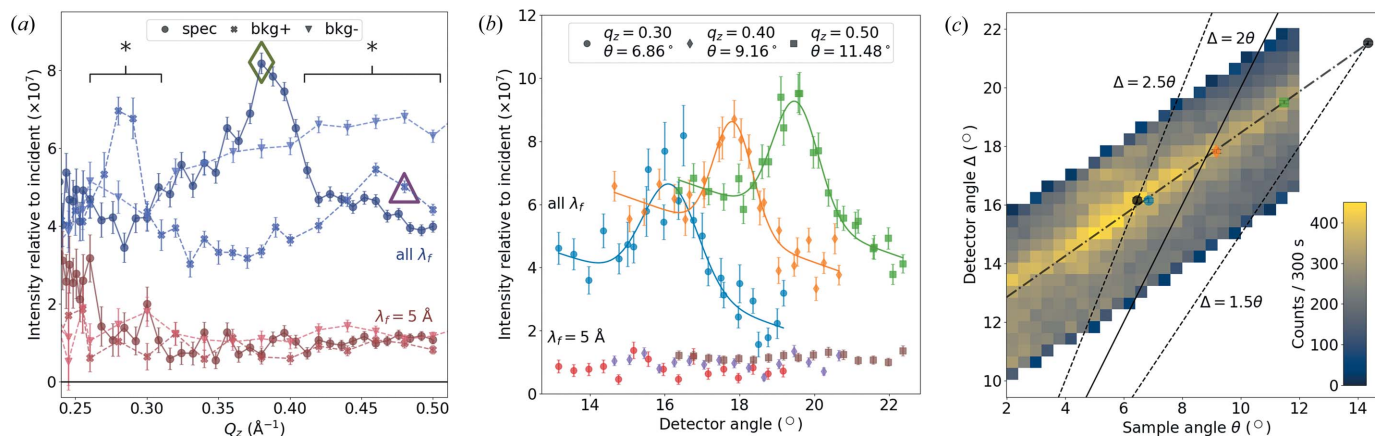
Figure 3
Observation of a spurious background peak (spurion). (a) High-Q_z neutron reflectivity of a rough thin film on a sample substrate mounted in air with $\gamma = 0°$. Measurements of the individual normalized specular (spec) and background (bkg+ and bkg−) intensities were performed with the MAGIK reflectometer with ($\lambda_f = 5$ Å) and without (all λ_f) energy-analyzed detection. The spurion peak is at $Q_z = 0.38$ Å^{-1}. Asterisks indicate regions where the background measurements are significantly higher than the specular signal. These features are not observed when the energy analyzer selects $\lambda_f = 5$ Å neutrons. Error bars represent 68% confidence intervals of the reduced data. (b) Detector (transverse) scans across the spurion peak in the specular condition (orange diamonds) and at off-specular positions (blue circles and green squares). The peak is not observed when the energy analyzer selects $\lambda_f = 5$ Å neutrons. Error bars represent 68% confidence intervals of the reduced data. (c) A color map showing the spurion ridge measured through the center of a large silicon block at $\gamma = 0°$. The solid line represents the specular ridge. Dashed lines show the positions of background measurements, and the black points show where the spurion is observed in the background intensities. The dashed–dotted line is a linear fit through the observed spurion peak locations from the thin-film sample in panels (a), (b) and corresponds well to the spurion ridge. Error bars represent the 68% confidence interval of the spurion peak location.

measurement [Fig. 2(a)]. Up to $Q_z \simeq 0.25$ Å^{-1}, the measured reflectivities are very similar; above this value, there are substantial deviations.

The solid lines show the calculated reflectivity from a single thin-film model optimized simultaneously to the D_2O and H_2O data using the *Refl1D* software (Kienzle *et al.*, 2021) (Table S1 in the supporting information). Of the data collected with the analyzer out, only the $Q_z < 0.25$ Å^{-1} region was used for the optimization. Comparison of the D_2O measurements with the expected reflectivity curves [Fig. 2(a)] shows that, when the analyzer is in, the reflectivity is consistent with the thin-film model over the entire Q_z range. When the analyzer is out, significant spurious reflectivity (near $Q_z \simeq 0.38$ Å^{-1}) and background oversubtraction (at $Q_z \simeq 0.28$ Å^{-1} and $Q_z \simeq 0.48$ Å^{-1}) are observed.

Inspection of the normalized intensities shown in the inset reveals peaks in I_{spec} and I_{bkg+} near $Q_z \simeq 0.4$ Å^{-1} and $Q_z \simeq 0.48$ Å^{-1}, respectively, when the analyzer is out. These interfere with background subtraction by interpolation and account for the observed structure in the reflectivity. These spurious peaks ('spurions') are absent from the $\lambda_f = 5$ Å data, for which background subtraction by interpolation performs admirably. This suggests a role for inelastic scattering in originating the spurions.

Fig. 2(b) and its inset show that similar problems exist with H_2O in the liquid cell. While the spurion peaks are more difficult to

observe over the high incoherent background from the H_2O reservoir, this measurement demonstrates that the spurions do not arise specifically from the presence of D_2O or the specific structure of the D_2O/SiO_2 interface.
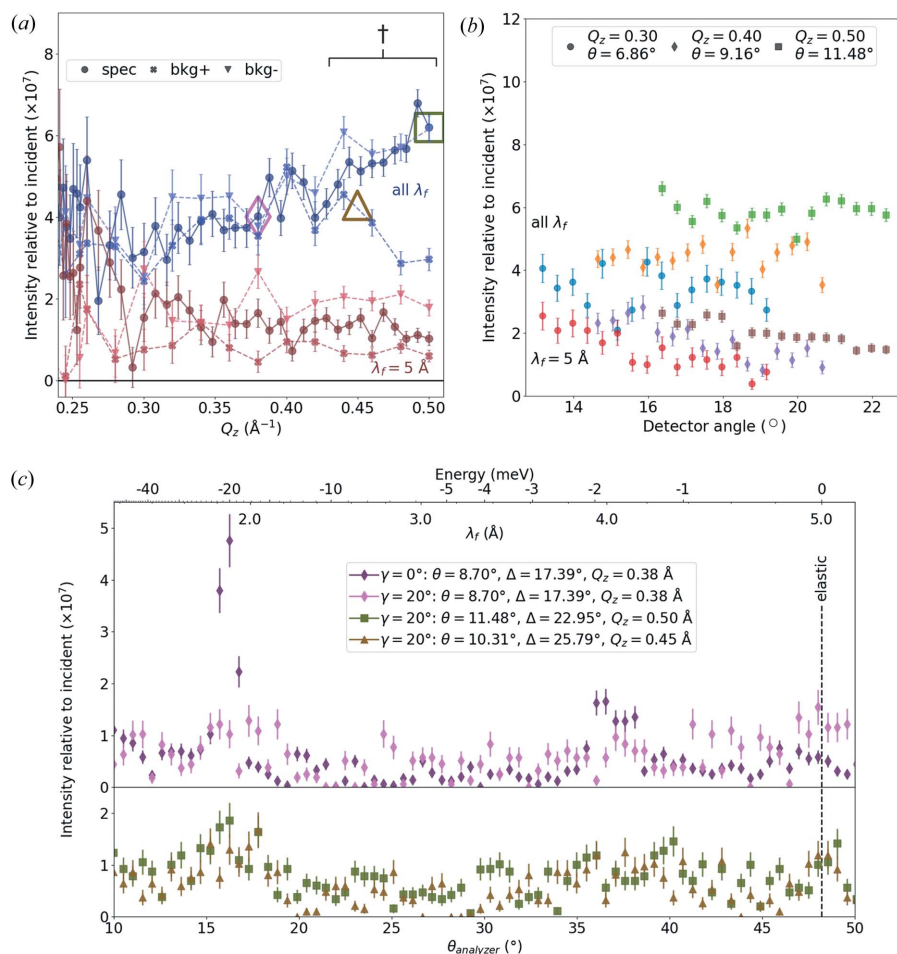
To determine any effect of the flow cell geometry, a similar measurement was performed on a different thin-film sample in air. This sample was chosen to have high roughness and thus poor specular reflectivity above $Q_z \simeq 0.25$ Å^{-1}. Fig. 3(a) shows
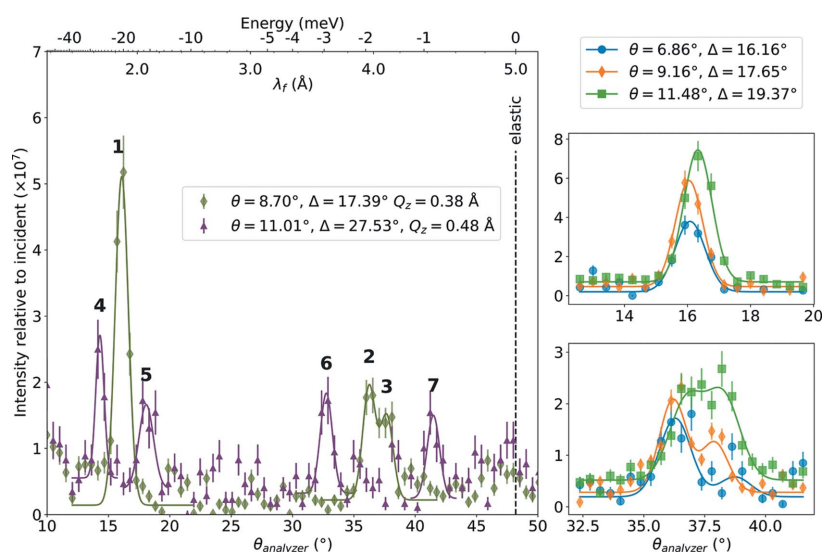
Figure 4
Energy spectrum of the spurion with $\gamma = 0°$. The spectra in the left-hand panel correspond by color and symbol to the large open symbols in Fig. 3(a), while the spectra in the right-hand panels correspond by color and symbol to the measurements at the peak positions in Fig. 3(b). Q_z values are nominal based on the sample angle. Error bars represent 68% confidence intervals of the reduced data.

the same features as the Fig. 2(a) inset, suggesting that the spurions arise from the silicon substrate rather than from interfacial effects or from the thin-film coating. This is supported by Fig. 3(b), where transverse scans of Δ for fixed θ show the same peak detected at different off-specular locations as well as at the specular ridge at $Q_z \simeq 0.38\ \text{Å}^{-1}$. The peaks are completely absent if the energy analyzer is installed. Importantly, the spurion peaks do not overlap in Δ; in this case, one might suspect an increased background from an environmental source that the detector sees only at a specific detector position.

The intensity map in Fig. 3(c) was measured using the MAGIK position-sensitive detector from a neutron beam passing through the center of a large silicon block aligned to the beam with $\gamma = 0°$ and shows that the spurion indeed forms a ridge that crosses the specular ridge near a nominal $Q_z \simeq 0.38\ \text{Å}^{-1}$. The maximum spurion peak positions reported in Fig. 3(b) are plotted as colored points, showing excellent agreement between the two samples.

To elucidate the scattering process that produces the spurion ridge, we configured the instrument at the position where the spurion and specular ridges cross [olive diamond in Fig. 3(a)], and then scanned λ_f. The results are shown by the matching olive diamonds in Fig. 4. The bottom horizontal axis shows θ_{analyzer}, while the top two axes show the wavelength of the detected neutrons and the energy change of the scattering process (a negative value indicates that energy was given to the scattered neutron). A large peak is observed at an energy of about −20 meV (4.8 THz), while a double peak is observed at an energy of about −2 meV. The solid lines are predictions of single or double Gaussian models with a constant background after optimization to the experimental data using a weighted Levenberg–Marquardt algorithm. The right-hand panels of Fig. 4 show details of these peaks for the three points indicated in Fig. 3(c), revealing little change along the spurion ridge. Off the spurion ridge, at $I_{\text{bkg+}}(0.48\ \text{Å}^{-1})$ [purple triangles in Figs. 3(a) and 4], where the background intensities are much higher than the specular intensities, the peaks appear to split but maintain the total intensities and approximate average energies.

It is suggestive that the 4.8 THz energy associated with the spurion is well represented in the band structure of silicon, near [110], while lower energy transfers are available at the Brillouin zone edges (Kulda *et al.*, 1994). We thus hypothesize that the spurion arises from a multiple scattering process involving phonon scattering coupled with a Bragg reflection from the crystal.

If this hypothesis is correct, then the results should look significantly different if the sample crystal is rotated so the beam is no longer incident along the [220] direction. Fig. 5(a) shows the same measurements as in Fig. 3(a) for the same sample crystal in air but rotated to $\gamma = 20°$. The spurion peaks disappear and the specular intensity is consistent with the background intensities out to a higher Q_z value of about 0.43 Å^{-1}, where the specular and background intensities again separate. The absence of the spurion peaks is particularly striking in the comparison of Fig. 5(b) ($\gamma = 20°$) and Fig. 3(b) ($\gamma = 0°$). Fig. 5(c) shows a comparison of the energy spectrum at various instrument configurations. The top panel shows a direct comparison of the energy spectrum for $\gamma = 0°$ and $\gamma = 20°$ at the specular condition, corresponding to $Q_z = 0.38\ \text{Å}^{-1}$. The −20 meV (4.8 THz) peak is much less sharp but still present, while the remainder of the inelastic background appears higher in the $\gamma = 20°$

Figure 5
The effect of rotating the sample from Figs. 3(a) and 3(b) to $\gamma = 20°$. (a) High-Q_z neutron reflectivity as in Fig. 3(a). The spurion peak is no longer observed, and new features appear above $Q_z = 0.45\ \text{Å}^{-1}$. (b) Transverse scans identical to those in Fig. 3(b). (c) The top panel compares spectra measured in the specular condition ($Q_z = 0.38\ \text{Å}^{-1}$) at $\gamma = 0°$ and $\gamma = 20°$, as shown by the purple and pink diamonds in Fig. 3(a) and panel (a), respectively. The bottom panel shows the energy spectra at the instrument configurations shown by the brown triangle and green square in panel (a). Q_z values are nominal based on the sample angle. Error bars represent 68% confidence intervals of the reduced data.

configuration; indeed, the integrated intensities in the θ_{analyzer} range from 10 to 45° are the same within the 68% confidence interval. The broad features of the energy spectrum persist in the other instrument configurations shown in the bottom panel of Fig. 5(c) and by matching symbols in Fig. 5(a).

4. Discussion

Low-background neutron reflectometry at high Q_z is of critical importance for improving the apparent spatial resolution of neutron reflectometry measurements. For electrochemical systems, improved resolution would allow detection of very thin surface layers (Dura et al., 1998). NR measurements of biological systems would particularly benefit, as discrimination of many structural features (e.g. α-helices of proteins, bilayer headgroup structure) requires sub-10 Å resolution. This is routinely realized in neutron diffraction studies (Mihailescu et al., 2019) but has not been achieved with any regularity in neutron reflectometry (Krueger et al., 2001).

The results presented here highlight three major challenges for routine high-resolution NR. First, and most fundamentally, NR signals at high Q_z are extremely small and thus require long counting times (or very bright sources) to measure. For high-resolution NR, the target reflectivity is approximately 10^{-8} (Krueger et al., 2001; Hoogerheide, Heinrich et al., 2020), with enough neutrons counted for the high-Q_z data to have a reasonable information content (Treece et al., 2019). For specularly reflected neutrons with rate r in the absence of background, assuming sufficient neutrons are counted that the Poisson rate distribution for a counting time t can be approximated by a Gaussian with variance $\delta r^2 t^2 = rt$, a precision $\alpha = \delta r / r$ is achieved in a time $t = (\alpha^2 r)^{-1}$.

Second, because the signal at high Q_z is so small, the signal-to-background ratio (SBR) is also small. Consider a background rate r_b, such that SBR = r/r_b. The rate of specular reflection r is determined by measuring the specular reflection signal in the presence of background $(r + r_b)$ and then subtracting the background rate, i.e. $r = (r + r_b) - r_b$. [This calculation assumes that no additional information can be brought to bear to reduce the uncertainty in r_b, as in background field subtraction techniques (Hoogerheide, Heinrich et al., 2020).] The variance of this determination for a counting time t, again assuming Gaussian statistics, is $\delta r^2 t^2 = \delta(r + r_b)^2 + \delta r_b^2 = (r + r_b)t + r_b t$, such that $\delta r^2 = t^{-1}(r + 2r_b)$. The counting time required to achieve a precision α is then

$$t = (\alpha^2 r)^{-1}\left(1 + \frac{2r_b}{r}\right) = (\alpha^2 r)^{-1}\left(1 + \frac{2}{\text{SBR}}\right). \quad (3)$$

Equation (3) demonstrates the intuitive result that, when SBR < 1 (the usual case at high Q_z), most of the counting time is spent accounting for the uncertainty in r_b. Importantly, in this regime the counting time decreases in direct proportion to the increase in the SBR (Fig. S2 in the supporting information).

Fig. 6 quantifies the effect of energy analysis on the SBR for the experiment shown in Fig. 2 using the liquid cell. Fig. 6(a) shows the factor by which the background is decreased by

moving the energy analyzer to the 'in' position, i.e. $I(\text{all } \lambda_f)/I(\lambda_f = 5 \text{ Å})$. This is the same as the ratio SBR($\lambda_f = 5 \text{ Å}$)/SBR(all λ_f) in the two conditions and thus corresponds to the improvement in counting time realized by using the energy analyzer. This is an improvement of a factor of 3 or more for samples in D_2O. However, the H_2O background remains dominated by elastic incoherent scattering and thus samples in H_2O will see a lesser improvement. Here, each of the D_2O and H_2O curves is the average of the background ratios determined for the specular and background normalized intensities.

The high-Q_z background arising from D_2O reservoirs using the energy analyzer [Fig. 2(a), inset] is approximately 4×10^{-7}. This is an acceptable background level identified by Hoogerheide, Heinrich et al. (2020) for high-resolution measurement and is achieved by a twofold reduction in the reservoir thickness and the introduction of energy-analyzed detection. Further reduction in reservoir thickness should be achievable, bringing the background level closer to 10^{-7} for lipid bilayers on silicon. Note that a background level of 10^{-7} is already achieved for silicon substrates in air [Fig. 3(a)], presumably because inelastically scattered neutrons account for a large fraction of scattering background from air and are effectively filtered by the energy analyzer (Barker & Mildner, 2015; Shirane et al., 2002).

The fraction of the background intensity that is filtered by energy analysis, i.e. $1 - I(\lambda_f = 5 \text{ Å})/I(\text{all } \lambda_f)$, approximates the fraction of background scattering that arises from inelastic processes. Fig. 6(b) demonstrates that about 80% of the background scattering from silicon arises from inelastic scattering, while at least 2/3 of the background from D_2O and 1/3 of the background from H_2O is inelastic in origin. These values are at least qualitatively consistent with time-of-flight (TOF) measurements of the inelastic background arising from these materials (Barker & Mildner, 2015). For the 'Si' curve, only specular-like data were used, but the sample was translated such that the beam passed only through the silicon substrate and did not impinge on the liquid reservoir or any reflective interfaces.
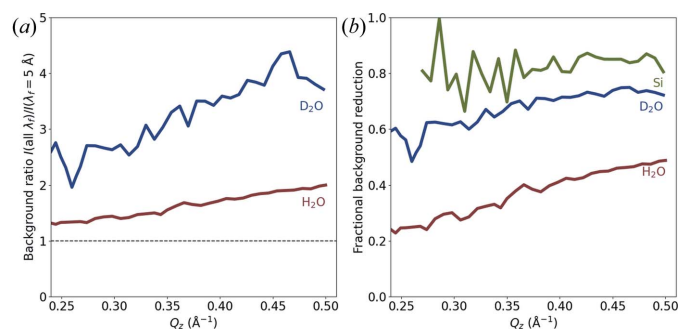
Figure 6
Background improvements from employing energy-analyzed detection, calculated from the data in Fig. 2. (a) The ratio of measured intensity-normalized background levels with the analyzer out and in. This ratio is equivalent to the ratio of signal-to-background ratios in the two conditions. (b) The fractional background reduction is a measure of how much scattering arises from inelastic processes in each material. Uncertainty (particularly in Si) arises from the very low count rates and can be estimated from the variation in neighboring points.

The third impediment to high-Q_z measurement is the non-isotropic nature of the inelastic contribution to the background. Any background subtraction scheme that relies on interpolation, including the linear interpolation scheme used here, or polynomial interpolation schemes that become available if a position-sensitive detector is used, risks introducing spurious structure into the measured reflectivity profile [Fig. 2(a)]. Similarly, background field subtraction assumes isotropic scattering (Hoogerheide, Heinrich *et al.*, 2020). In addition, because the cross sections for these processes are small and multiple scattering events (*e.g.* phonon + Bragg scattering) are involved, it is difficult to predict *a priori* where spurions will occur. Previous measurements of the inelastic scattering from 220 Si using TOF small-angle neutron scattering show a complex inelastic landscape at high Q_z (Barker & Mildner, 2015). Comparison of Fig. 3 with Fig. 5, similarly, shows that large features such as the $Q_z = 0.38$ Å^{-1} spurion at $\gamma = 0°$ can be avoided by γ rotations; but in this case large pathological features are instead shifted to a different (in this case higher) Q_z value, and it remains unclear whether any structure at lower Q_z arises from these sorts of systematic errors or true elastic specular reflection. For the large rectangular silicon blocks in widespread use worldwide for liquid cells, however, it may be valuable to explore the inelastic scattering landscape as a function of γ and subsequently miscut the silicon blocks at an advantageous angle. Finally, the Q_z value at which spurions affect the specular reflectivity will be highly wavelength dependent.

A formula for low-background high-resolution neutron reflectometry thus has three components: high-flux beams, low intrinsic background measurements and reduction of systematic errors introduced by non-isotropic inelastic scattering. Previously, we had shown that reducing the liquid reservoir thickness has a strong effect on the intrinsic background (Hoogerheide, Heinrich *et al.*, 2020). In this paper, we use a liquid cell with a thin reservoir to demonstrate further that energy analysis of scattered neutrons both reduces systematic errors from structured inelastic scattering and reduces the intrinsic background from the liquid reservoir. The final challenge is high flux. At continuous sources, this can be achieved on instruments such as the CANDOR reflectometer [Fig. 1(b)] by multiplexing. Crucially, CANDOR also features energy-analyzed detection.

The dramatic effect of combining a high-flux instrument with low-background liquid cell design and energy-analyzed neutron detection is shown in Fig. 7. Here, the measurement of the D_2O-containing liquid cell on MAGIK with the energy analyzer in [reproduced from Fig. 2(a)] is compared with the same measurement on the CANDOR reflectometer in half the time. Solid curves are the predictions of the single thin-film models described previously after optimization to each data set. As shown in the inset, the CANDOR reflectometer resolves a neutron reflectivity of 10^{-8} at $Q_z = 0.4$ Å^{-1} in a reasonable experiment time, whereas the monochromatic MAGIK reflectometer resolves $R \simeq 10^{-7}$ at $Q_z \simeq 0.28$ Å^{-1}.

The methods described here are generally applicable to background reduction for monochromatic reflectometers at
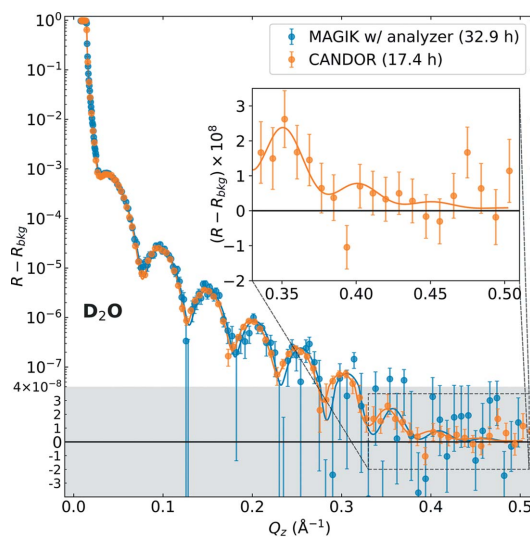

Figure 7
A comparison of energy-analyzed measurements of the same liquid cell as in Fig. 2(a) with MAGIK and CANDOR. Shaded areas are plotted on a linear scale. (Inset) Detail of the high-Q_z region from the CANDOR measurement, demonstrating peaks resolved at the sub-10^{-8} level. Solid curves are the result of optimizing the single thin-film model to the experimental data. Error bars represent 68% confidence intervals of the reduced data.

reactor sources. Installing an energy analyzer at the detector position that mirrors the source monochromator will give a significant improvement in the SBR. Multiplexing instruments such as CANDOR designed to combine the advantages of continuous sources and simultaneous wavelength-discriminated measurement will also be invaluable. For TOF-based instrumentation at pulsed neutron sources, investigating whether averaging over multiple wavelengths mitigates the effects of spurions or introduces artifacts that require correction is likely to be a profitable area for future study.

5. Summary

In summary, we have demonstrated high-resolution low-background neutron reflectometry at the 10^{-8} level from a liquid cell in reasonable experimental counting times of <18 h by improving conventional experiments in three ways: first, in a cell otherwise made entirely of single-crystal silicon, reducing the liquid reservoir thickness below 50 µm; second, deploying energy-analyzed detection both to reduce the isotropic inelastic background scattering from the liquid reservoir and to remove non-isotropic inelastic artifacts arising from the single-crystal silicon; and third, performing the experiment with the high-flux CANDOR reflectometer. The measurements reported here also show significant improvements in signal-to-background ratio for monochromatic reflectometers at continuous neutron sources using post-sample energy-analyzed detection.

Acknowledgements

the CANDOR engineering and electronics teams. Access to CANDOR was provided by the Center for High Resolution Neutron Scattering, a partnership between the National Institute of Standards and Technology and the National Science Foundation under agreement No. DMR-2010792. The authors thank Peter Litwinowicz at the Center for Nanoscale Science and Technology at the National Institute of Standards and Technology, US Department of Commerce, for performing the sputtered thin-film depositions. Certain commercial materials, equipment and instruments are identified in this work to describe the experimental procedure as completely as possible. In no case does such an identification imply a recommendation or endorsement by NIST, nor does it imply that the materials, equipment or instruments identified are necessarily the best available for the purpose.

References

Ankner, J. F., Heller, W. T., Herwig, K. W., Meilleur, F. & Myles, D. A. A. (2013). *Curr. Protoc. Protein Sci.* **72**, 17.

Barker, J. G. & Mildner, D. F. R. (2015). *J. Appl. Cryst.* **48**, 1055–1071.

Berk, N. F. & Majkrzak, C. F. (2003). *Langmuir*, **19**, 7811–7817.

Clifton, L. A., Paracini, N., Hughes, A. V., Lakey, J. H., Steinke, N.-J., Cooper, J. F. K., Gavutis, M. & Skoda, M. W. A. (2019). *Langmuir*, **35**, 13735–13744.

Dura, J. A., Pierce, D. J., Majkrzak, C. F., Maliszewskyj, N. C., McGillivray, D. J., Lösche, M., O'Donovan, K. V., Mihailescu, M., Perez-Salas, U., Worcester, D. L. & White, S. H. (2006). *Rev. Sci. Instrum.* **77**, 074301.

Dura, J. A., Richter, C. A., Majkrzak, C. F. & Nguyen, N. V. (1998). *Appl. Phys. Lett.* **73**, 2131–2133.

Dura, J. A., Rus, E. D., Kienzle, P. A. & Maranville, B. B. (2017). *Nanolayer Research – Methodology and Technology for Green Chemistry*, edited by T. Imae, ch. 5, pp. 155–202. Amsterdam: Elsevier.

Eells, R., Hoogerheide, D. P., Kienzle, P. A., Lösche, M., Majkrzak, C. F. & Heinrich, F. (2019). *Characterization of Biological Membranes – Structure and Dynamics*, edited by M.-P. Nieh, F. A. Heberle & J. Katsaras, ch. 3, pp. 87–130. Berlin: de Gruyter.

Fitter, J., Gutberlet, T. & Katsaras, J. (2006). Editors. *Neutron Scattering in Biology: Techniques and Applications*. Berlin, Heidelberg: Springer.

Fragneto, G., Charitat, T., Graner, F., Mecke, K., Perino-Gallice, L. & Bellet-Amalric, E. (2001). *Europhys. Lett.* **53**, 100–106.

Heinrich, F. & Lösche, M. (2014). *Biochim. Biophys. Acta*, **1838**, 2341–2349.

Hoogerheide, D. P., Forsyth, V. T. & Brown, K. A. (2020). *Phys. Today*, **73**, 36–42.

Hoogerheide, D. P., Heinrich, F., Maranville, B. B. & Majkrzak, C. F. (2020). *J. Appl. Cryst.* **53**, 15–26.

Hoogerheide, D. P., Noskov, S. Y., Jacobs, D., Bergdoll, L., Silin, V., Worcester, D. L., Abramson, J., Nanda, H., Rostovtseva, T. K. & Bezrukov, S. M. (2017). *Proc. Natl Acad. Sci. USA*, **114**, E3622–E3631.

Hoogerheide, D. P., Noskov, S. Y., Kuszak, A. J., Buchanan, S. K., Rostovtseva, T. K. & Nanda, H. (2018). *Acta Cryst.* D**74**, 1219–1232.

Junghans, A., Watkins, E. B., Barker, R. D., Singh, S., Waltman, M. J., Smith, H. L., Pocivavsek, L. & Majewski, J. (2015). *Biointerphases*, **10**, 019014.

Kienzle, P. A., Krycka, J., Patel, N., Metting, C., Sahin, I., Fu, Z., Chen, W., Mont, A. & Tighe, D. (2021). *Refl1D*. Version 0.8.14. https://www.nist.gov/ncnr/reflectometry-software.

Kopetka, P. A., Williams, R. E. & Rowe, J. M. (2006). Report NISTIR 7352. National Institute of Standards, Gaithersburg, MD, USA.

Krueger, S., Meuse, C. W., Majkrzak, C. F., Dura, J. A., Berk, N. F., Tarek, M. & Plant, A. L. (2001). *Langmuir*, **17**, 511–521.

Kulda, J., Strauch, D., Pavone, P. & Ishii, Y. (1994). *Phys. Rev. B*, **50**, 13347–13354.

Majkrzak, C. F., Berk, N. F. & Perez-Salas, U. A. (2003). *Langmuir*, **19**, 7796–7810.

Maliszewskyj, N. C., Osovizky, A., Pritchard, K., Yehuda-Zada, Y., Binkley, E., Ziegler, J., Tsai, P., Hadad, N., Baltic, G. M., Jackson, M., Hurlbut, C. & Majkrzak, C. F. (2018). *Nucl. Instrum. Methods Phys. Res. A*, **907**, 90–96.

Maranville, B., Ratcliff, W. II & Kienzle, P. (2018). *J. Appl. Cryst.* **51**, 1500–1506.

McGillivray, D. J., Valincius, G., Heinrich, F., Robertson, J. W., Vanderah, D. J., Febo-Ayala, W., Ignatjev, I., Lösche, M. & Kasianowicz, J. J. (2009). *Biophys. J.* **96**, 1547–1553.

Michalak, D. J., Lösche, M. & Hoogerheide, D. P. (2021). *Langmuir*, **37**, 3970–3981.

Mihailescu, M., Sorci, M., Seckute, J., Silin, V. I., Hammer, J., Perrin, B. S., Hernandez, J. I., Smajic, N., Shrestha, A., Bogardus, K. A., Greenwood, A. I., Fu, R., Blazyk, J., Pastor, R. W., Nicholson, L. K., Belfort, G. & Cotten, M. L. (2019). *J. Am. Chem. Soc.* **141**, 9837–9853.

Nylander, T., Campbell, R. A., Vandoolaeghe, P., Cárdenas, M., Linse, P. & Rennie, A. R. (2008). *Biointerphases*, **3**, FB64–FB82.

Owejan, J. E., Owejan, J. P., DeCaluwe, S. C. & Dura, J. A. (2012). *Chem. Mater.* **24**, 2133–2140.

Paracini, N., Clifton, L. A., Skoda, M. W. A. & Lakey, J. H. (2018). *Proc. Natl Acad. Sci. USA*, **115**, E7587–E7594.

Pfefferkorn, C. M., Heinrich, F., Sodt, A. J., Maltsev, A. S., Pastor, R. W. & Lee, J. C. (2012). *Biophys. J.* **102**, 613–621.

Pritchard, K., Osovizky, A., Ziegler, J., Binkley, E., Tsai, P., Hadad, N., Jackson, M., Hurlbut, C., Baltic, G. M., Majkrzak, C. F. & Maliszewskyj, N. C. (2020). *IEEE Trans. Nucl. Sci.* **67**, 414–421.

Rus, E. D. & Dura, J. A. (2019). *Appl. Mater. Interfaces*, **11**, 47553–47563.

Schalke, M. & Lösche, M. (2000). *Adv. Colloid Interface Sci.* **88**, 243–274.

Sears, V. F. (1992). *Neutron News*, **3**(3), 26–37.

Shirane, G., Shapiro, S. M. & Tranquada, J. M. (2002). *Neutron Scattering with a Triple-Axis Spectrometer: Basic Techniques.* Cambridge University Press.

Silin, V. I. & Hoogerheide, D. P. (2021). *J. Colloid Interface Sci.* **594**, 279–289.

Soranzo, T., Martin, D. K., Lenormand, J.-L. & Watkins, E. B. (2017). *Sci. Rep.* **7**, 3399.

Soubias, O., Pant, S., Heinrich, F., Zhang, Y., Roy, N. S., Li, J., Jian, X., Yohe, M. E., Randazzo, P. A., Lösche, M., Tajkhorshid, E. & Byrd, R. A. (2020). *Sci. Adv.* **6**, eabd1882.

Thorsen, M. K., Lai, A., Lee, M. W., Hoogerheide, D. P., Wong, G. C. L., Freed, J. H. & Heldwein, E. E. (2021). *mBio*, **12**, e01548–01521.

Treece, B. W., Kienzle, P. A., Hoogerheide, D. P., Majkrzak, C. F., Lösche, M. & Heinrich, F. (2019). *J. Appl. Cryst.* **52**, 47–59.

Van, Q. N., López, C. A., Tonelli, M., Taylor, T., Niu, B., Stanley, C. B., Bhowmik, D., Tran, T. H., Frank, P. H., Messing, S., Alexander, P., Scott, D., Ye, X., Drew, M., Chertov, O., Lösche, M., Ramanathan, A., Gross, M. L., Hengartner, N. W., Westler, W. M., Markley, J. L., Simanshu, D. K., Nissley, D. V., Gillette, W. K., Esposito, D., McCormick, F., Gnanakaran, S., Heinrich, F. & Stephen, A. G. (2020). *Proc. Natl Acad. Sci. USA*, **117**, 24258–24268.